Dynamic Assembly of Magnetic Colloidal Vortices

Tomaž Mohorič,[†,‡] Gašper Kokot,[§] Natan Osterman,[§] Alexey Snezhko,[∥] Andrej Vilfan,[§] Dušan Babič,[⊥] and Jure Dobnikar*[,†,#]

[†]International Research Center for Soft Matter, Beijing University of Chemical Technology, Beijing 100029, P.R. China

[‡]Department of Chemistry, University of Ljubljana, Večna pot 113, 1000 Ljubljana, Slovenia

[⊥]Department of Mathematics and Physics, Jadranska 19, 1000 Ljubljana, Slovenia

[§]Jožef Stefan Institute, Jamova cesta 39, 1000 Ljubljana, Slovenia

[∥]Argonne National Laboratory, 9700 Cass Avenue, Lemont, Illinois 60439, United States

[#]Department of Chemistry, University of Cambridge, Cambridge CB2 1TN, United Kingdom

S *Supporting Information*

ABSTRACT: Magnetic colloids in external time-dependent fields are subject to complex induced many-body interactions governing their self-assembly into a variety of equilibrium and out-of-equilibrium structures such as chains, networks, suspended membranes, and colloidal foams. Here, we report experiments, simulations, and theory probing the dynamic assembly of superparamagnetic colloids in precessing external magnetic fields. Within a range of field frequencies, we observe dynamic large-scale structures such as ordered phases composed of precessing chains, ribbons, and rotating fluidic vortices. We show that the structure formation is inherently coupled to the buildup of torque, which originates from internal relaxation of induced dipoles and from transient correlations among the particles as a result of short-lived chain formation. We discuss in detail the physical properties of the vortex phase and demonstrate its potential in particle-coating applications.
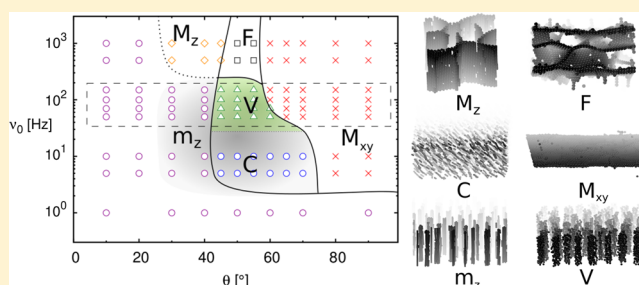
INTRODUCTION

The self-assembly process is one of the major routes toward designing novel functional materials. Superparamagnetic colloids in external fields have been extensively studied in this context.[1−19] Precessing magnetic fields can drive the aggregation of magnetic colloids into complex equilibrium structures in both 3D[4−7,17,20−22] and 2D[8−12,23] that can be explained by correctly incorporating many-body interactions. Magnetic chains, networks, membranes, or foams are observed in static fields or under periodic external driving with high frequencies where colloidal interactions are effectively time-averaged. The structures exhibit a rich diversity as a result of the many-body nature of the magnetic interactions. This underlying complexity often also implies that kinetic barriers have to be overcome[24] in order to actually assemble the desired structures. The design of new materials therefore involves understanding both the structure and the kinetics of their formation. Out-of-equilibrium dynamics, apart from providing access to novel structures, reveals the true (and much less explored) complexity of the systems.

In systems driven out of equilibrium by time-dependent external fields, emerging phenomena such as coherent large-scale self-organized structures of colloidal particles that exist only as a result of energy dissipation were recently reported.[1−3,8−11,25−27] Dynamic advection lattices[28] and lifelike

collective dynamics[1] have been studied in a suspension of magnetic platelets subjected to complex multiaxial magnetic fields, and unconventionally ordered dynamic architectures (magnetic snakes,[29] asters,[30] and spinners[11]) and self-propelling entities[8] have been discovered in magnetic colloidal ensembles suspended at liquid−air and liquid−liquid interfaces and energized by alternating magnetic fields. Synchronization has recently been explored as a tool toward self-assembly: magnetic Janus particles in precessing external fields organized into rotating tubes dynamically synchronized with the motion of the particles in a way reminiscent of the tidal locking of the Moon and Earth.[27] In the above examples, the particles self-assembled into the novel structures as a result of the delicate synchronization of their interactions, the external field, and the forces mediated by the solution. The so-called dynamic assembly,[31] i.e., dissipative self-assembly process enabled exclusively by the dynamics, brings to light novel complex phases that cannot be accessed via standard self-assembly procedures following the free-energy minimization. Interestingly, ferrofluid droplets were demonstrated to exhibit three regimes of self-assembly: equilibrium, kinetically trapped
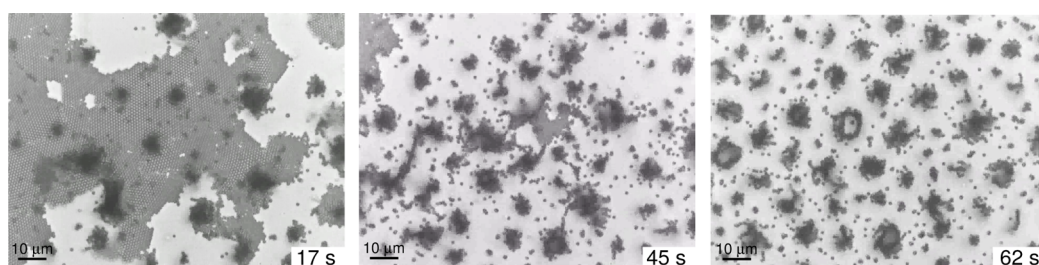
Figure 1. Emergent dynamics. The destabilization of a membrane upon switching the field mode and the subsequent formation of a dynamic phase of ordered rotating vortices. Experimental snapshots were obtained at field frequency $\nu_0 = 200$ Hz. Initially, the membrane was prepared in the external field of magnitude $B_0 = 4.32$ mT and opening angle $\theta = 55°$, just above the magic angle. The direction of precession was flipped after every period. At time zero, the flipping was turned off, and at the same time, the field opening angle was slightly decreased to $\theta = 53°$ ($B_0 = 4.44$ mT) in order to support alignment in the z direction and facilitate the observation.

nonequilibrium, and dissipative.[32] Biology is also abundant with all three processes: whereas some proteins fold into equilibrium structures and others into kinetically trapped structures, most of the cellular organization is governed by active, dissipative dynamics.[33] Finally, understanding the mechanisms of dynamic assembly is a key to advanced nonequilibrium strategies for materials design.[24,34]

We report experiments and simulations probing the dynamic assembly and emergent collective behavior of superparamagnetic colloids in precessing magnetic fields. Superparamagnetic particles are composite structures with iron oxide nanoparticles (8 nm) embedded in a polymer matrix and evenly dispersed throughout the volume of the microparticle, although some clustering is present. The magnetic moment of monodomain nanoparticles can randomly flip as a result of thermal fluctuations, leading to zero average magnetization in the absence of an external magnetic field. In an external field, the magnetic moments in monodomain nanoparticles collectively reorient, resulting in a net magnetization in the field direction.

Our experimental setup (described in detail in Materials and Methods section) is similar to the one in ref 17, where the precessing magnetic field was applied to drive the aggregation of colloids into self-healing membranes. In ref 17, the field was precessing close to the so-called magic angle at a relatively high frequency (200 Hz). In order to avoid any net rotation of colloidal assemblies, the direction of the field rotation was flipped every period. Hence, the induced magnetic interactions were correctly captured in a time-averaged way, and no net fluid flow causing complex hydrodynamic effects had to be considered to understand the stability of the observed steady-state structures.

Here, we chose to study the opposite scenario: external field precessing with a constant sense of rotation. In such a case, we observe a net physical rotation of colloidal particles and their assemblies. The dynamics of a single particle in a rotating magnetic field is determined by both the magnetic anisotropy of a particle and the relaxation dynamics of the internal degrees of freedom and is already complex, as is evident from the broad distribution of relaxation times.[35] At low frequencies (up to around 1 Hz), the anisotropy axis of the particle locks with respect to the rotating field. In the intermediate regime (around 10 Hz), the particles do not follow the rotation of the field and phase slippage occurs, but the anisotropy still results in directed rotation with a frequency smaller than that of the external field. At higher frequencies (100 Hz and above), the relaxation dynamics leads to a lag angle between the rotating field and the induced magnetization and results in a net torque on the

particle. The rotational frequency saturates at a few hertz, depending on the field strength.

In particle clusters, such dynamics is even more complex because of the many-body effects. Specifically, the field can induce a deformation of the cluster that lags behind the rotating field.[13] The angle between the symmetry plane of a cluster and the field results in an additional torque. In addition to the large-scale deformations, short-range inhomogeneities in which pairs of particles or small chains follow the rotation of the field can also be a source of torque, similar to a paramagnetic ellipsoid in a precessing field.[36]

The emergent behavior therefore depends on the frequency of the external field: at very low frequencies, the situation is quasi-static, but at very high frequencies (much faster than the relaxation processes), the magnetic interactions become time-averaged. The focus of this work is on the intermediate range of frequencies where the colloidal assembly is inherently coupled to the dynamics[1–3,13,26,27] and the time-averaged interactions cannot correctly capture their emergent behavior. In addition, the torque induced by the rotating field destabilizes some of the static structures, thus introducing a further level of complexity. Within the range of parameters of external energy injection studied in this work, we observe a variety of novel dynamically stabilized structures such as precessing chains, rotating membrane patches, and ordered arrays of rotating fluidic vortices.

■ VORTEX PHASE

To start with, we observe a drastic effect in the following experiment: The system is initially prepared in the same way as in ref 17, i.e., the external field precesses at approximately the magic angle of $\theta_m = 54.7°$ with frequency $\nu_0 = 200$ Hz. The direction of precession is flipped every period, and as a consequence, the colloids assemble into a single-particle-thick close-packed hexagonal membrane. Once this is achieved, we stop flipping the direction of the field rotation while keeping all other parameters unchanged. Surprisingly, roughly within a minute, the membrane completely dissolves and the colloids arrange into an ordered array of rotating vortices. The vortices are stable, similar in size, and rotate with frequencies on the order of 1 Hz. However, if we reverse the process and start flipping the field direction again, then the vortices stop rotating and slowly degrade. The snapshots in Figure 1 and movies S1 and S2 in the Supporting Information depict this intriguing behavior.

The decisive difference between the initial (membranes) and final (vortices) states is that in the final state a torque causes the physical rotation of colloidal particles and their assemblies. In

the middle of a membrane, the evenly distributed torque does not cause a net force, but it does so at its edges or around defects. This is confirmed (Figure 1 and movie S1) by the observation that membranes typically start disassembling at the edges and the instability spreads from there to the inside. Once rotating clusters start forming, repulsive magnetic intercluster interactions in combination with the fluid flow, which is also repulsive (due to many-body effects,[37] elastic deformations,[38] and inertial effects[39,40]), eventually arrange them on a hexagonal lattice (see vortex−vortex triplet correlation functions in Figure S1 in the SI). In the steady state, the magnetic torque on a single vortex is counterbalanced by viscous drag, which results in vortex rotation at a constant frequency.

■ PHASE DIAGRAM

The vortex phase is observed in a narrow range of opening angles θ of the precessing magnetic field. In the experiments, we explored the behavior of the system within a wider range of parameters and mapped out the dynamic phase diagram. We observed 2D snapshots that are cuts through the system along the focal plane of the microscope. Typical snapshots observed are displayed in Figure 2. We can probe the 3D structure of the
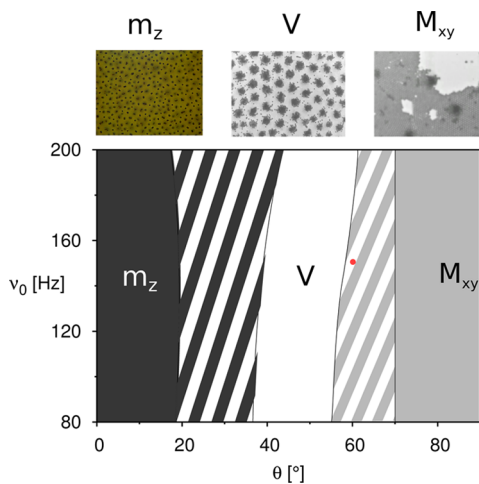
Figure 2. Dynamic phase diagram obtained from the experiments at magnetic field magnitude B_0 = 4 mT. Representative experimental snapshots for distinct phases are depicted above: ribbons m_z, vortices V, and membranes M_{xy}. The regions of phase coexistence are denoted with stripes. The red dot marks the hysteresis, i.e., the persistence of the vortex phase if we start within the vortex phase, e.g., at 150 Hz and 50°, and slowly increase the field opening angle at a fixed frequency.

system to some extent by varying the focal plane, although this is usually hampered by the nontransparency of the magnetic particles. We probed frequency ν_0 between 80 and 200 Hz and opening angles from 0 to 90°. To a large extent, the state of the system is determined by θ, whereas, in the explored range, we observe only a weak dependence on the frequency. Increasing the opening angle θ from 0 to 90°, we observe the following structures: finite-sized ribbons rotating around the z axis (denoted by m_z; appearing as finite chains in 2D snapshots), vortices rotating around the z axis (V), and sheets with a hexagonal structure lying in the xy plane (M_{xy}). There are typically broad coexistence regions between the states, and the transition between them depends on the specific path chosen in the experiments, i.e., on the initial conditions. In the phase

diagram in Figure 2, the initial state was a suspension of randomly dispersed colloids. However, when starting from an already-formed vortex phase, its stability is extended into the coexistence region at a larger value of θ (red dot in Figure 2).

The density dependence of the phase behavior has not been explored in full detail, but a quick probe of it reveals the following: if the local density is low, then the ribbons can be only one particle wide, i.e., chains on average oriented in the z direction with tips describing a circle in the xy plane; in 2D snapshots they appear as single particles with a halo coming from the rest of the chain, which is out of focus. Furthermore, the size of the vortices in the vortex phase grows with the overall density of colloids faster than their spacing. Therefore, at very high densities the vortices cease to be isolated and start exchanging their material (supplementary video S3 in the SI). The same happens if we decrease B_0 in a formed vortex phase. The vortices become increasingly lax, and eventually it is difficult to define them as separate clusters.

Further insight into the phase behavior is obtained by simulations where a broader range of parameters can be explored and the 3D structures of the observed phases are characterized with better accuracy. We performed Langevin dynamics simulations with a coarse-grained model incorporating many-body magnetic interactions and simple Stokes hydrodynamic drag. (The details of experiments and simulations are described in the Materials and Methods section.) The dynamic phase diagram determined by simulations is presented in Figure 3 as a function of frequency ν_0 and opening angle θ for a fixed magnitude of the magnetic field B_0 = 4 mT.

In a large part of the phase diagram, we observe static or quasi-static structures. At $\theta \approx 0°$, the external field is static and stable structures can be obtained by minimizing the interaction energy. We confirm that equilibrium phase m_z is indeed composed of finite-sized ribbons (Figure S2 in the SI). At finite θ and low frequencies, the time scale of colloidal rearrangement is much shorter than the period of field rotation. In this quasi-static regime, we observe ribbons precessing in phase with the external field. At the other extreme (high frequencies), the colloids cannot follow the field rotation and the interactions are time-averaged. In this regime, we observe the following structures: ribbons (m_z) and vertical membranes (M_z) at $\theta \lesssim 45°$, planar membranes (M_{xy}) at $\theta \gtrsim 60°$, and a magnetic foam phase (F) at values around the magic angle $\theta \approx \theta_m$ = 54.7°. The stability of the membranes can be explained by many-body interactions,[4,5,17] and their orientation by the time-averaged ratio of magnetic field components B_{0z}/B_{0xy}. The emergence of foam phase F is rationalized by the restored symmetry at the magic angle[4,5,17,21,22] where no spatial direction is preferred.

In the intermediate regime of frequencies and opening angles (shaded gray in Figure 3), the collective colloidal dynamics is coupled with the field, resulting in dynamic phases with no equilibrium counterparts. The vortex phase (V, shaded green) is observed at frequencies of $\nu_0 \approx 100$ Hz and $\theta \approx \theta_m$. At smaller θ, we observe rotating ribbons (m_z), and at $\theta \approx \theta_m$ and slightly smaller ν_0, we observe precessing chains (C). The range of frequencies in the experiment (Figure 2) is narrower and is marked by a dashed box in Figure 3. Within this region, we indeed confirm the weak frequency dependence and the observed sequence of structures upon varying θ as reported in the experiments.

Both in the experiments and in the simulations, the observed structures depend on the initial conditions, particularly in the
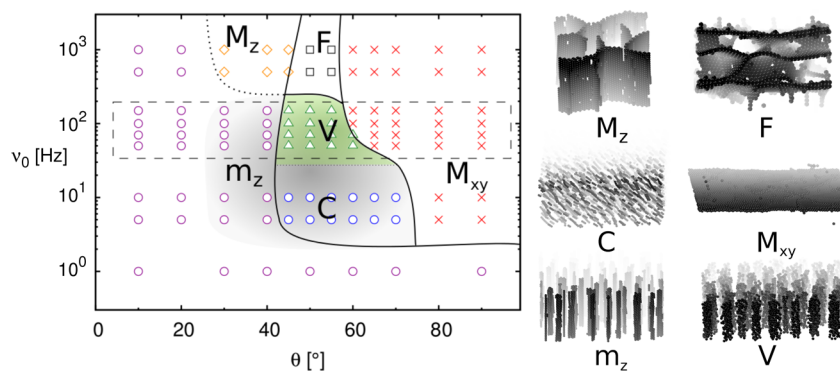
Figure 3. Dynamic phase diagram obtained by Langevin dynamics simulations. Different observed phases are marked: precessing ribbons m_z, vertical membranes M_z, magnetic foam F, vortex phase V (shaded green), precessing chains C, and planar membranes M_{xy}. The corresponding simulation snapshots are displayed. The approximate phase boundaries are drawn. The part of the phase diagram where the assembly is dynamically driven is shaded gray. The dashed box indicates the parameter region explored in the experiment (Figure 2).

region of dynamic assembly. In the experiments, the sensitivity to the initial conditions is reflected in the broad coexistence regimes (Figure 2). In the simulations, we observed that the characteristic size of the vortex depends on whether we start from a membrane or from a uniform random distribution. This is a major difference between equilibrium and dynamic phase behavior and is inherent in the complexity of the system.

■ SINGLE VORTEX DYNAMICS

In what follows, we focus on understanding the stability and dynamics of the vortex phase. Hydrodynamic interaction with its neighbors does not play a significant role in the dynamics of a vortex, which is best seen in the Supporting Information (video S4 and Figure S3), where a large isolated vortex is drifting close to static nonmagnetic pillars. We observe that the pillars do not visibly influence the vortex trajectory until the point of physical contact, when some of the outer layer particles are stripped off. Therefore, the long-range hydrodynamic interactions can be neglected when describing the dynamics of an individual vortex, and we will study it as isolated in the following.

We conducted a series of experiments and simulations where the vortex phase was first formed under reference conditions and then by slowly varying the opening angle of the precessing field θ and its frequency ν_0 and magnitude B_0. The experimental and simulation results are jointly presented in Figure 4. We observe that vortex cross-section A_v increases somewhat with the opening angle, which means that the vortices flatten out when the precessing field approaches or even crosses magic angle θ_m. There is no significant dependence of A_v on the field frequency and magnitude. The deviations of the simulation results at low frequencies and at large field strengths are due to the formation of chains, which results in swelling of the clusters due to the repulsive interchain magnetic interactions. However, intracluster hydrodynamic effects, not taken into account here, are likely to limit the effect of such phenomena. Vortex rotational frequency ν_v, on the other hand, is independent of field angle θ and frequency ν_0 but shows a strong dependence on field magnitude B_0. Because of the ambiguity in defining the average frequency in the simulations (Materials and Methods), we evaluated it in two ways: as an average over all of the particles in the vortex (red empty triangles) and as an average over the outermost shell of the particle (red full triangles). Qualitatively, there is agreement between the experiments and simulations, despite the fact that
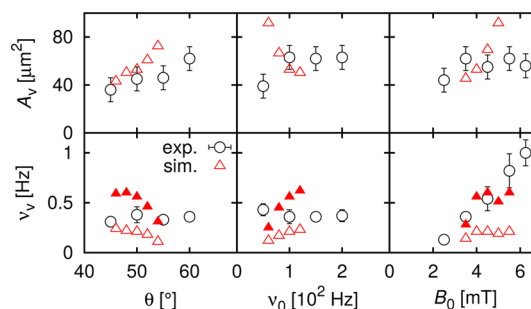
Figure 4. Vortex properties. Vortex cross-section A_v (top row) and frequency of vortex rotation ν_v (bottom row) as a function of the properties of the external field. Experimental (black circles) and simulational (red triangles) data are compared. Vortices were initially prepared under the reference conditions ($B_0 = 4$ mT, $\theta = 50°$, $\nu_0 = 100$ Hz). A single parameter was subsequently slowly varied, while the other two were kept under the reference conditions. The experimental points were obtained by averaging the properties over a large number (>1000) of vortices. The simulations were carried out with a single vortex containing $N = 436$ particles. Two protocols to evaluate ν_v in the simulations are used: an average over all particles within the vortex (empty triangles) and an average over particles at the vortex outer shell (full triangles).

in the simulation model only one of the relevant mechanisms responsible for the vortex rotation has been included. (See the theoretical model and the discussion in the next section.)

We can exploit the simulation to obtain further insights into the vortex dynamics that are inaccessible to direct experimental observation. We studied the stability of vortices of various sizes by following their time evolution (Figure 5A and Figures S4 and S5 in the SI). Sufficiently small vortices remain stable and homogeneous, but larger ones either form a hollow cylinder (sometimes with another tiny vortex in the center) or disintegrate into smaller vortices. All of these structures have been observed in the experiments where the formation of a hollow cylinder was found to be a precursor to structural instability (Figure S4 and video S5 in the SI). In fact, it is possible to experimentally achieve larger vortices (as in video S4) if we introduce a rigid center, e.g., a large rigid particle or agglomerate in the middle of the vortex. The vortex structure is not ordered, and its rotation is far more complex than that of a rigid body. The fluidic nature of the vortices is illustrated by the two trajectories with very similar initial conditions that diverge
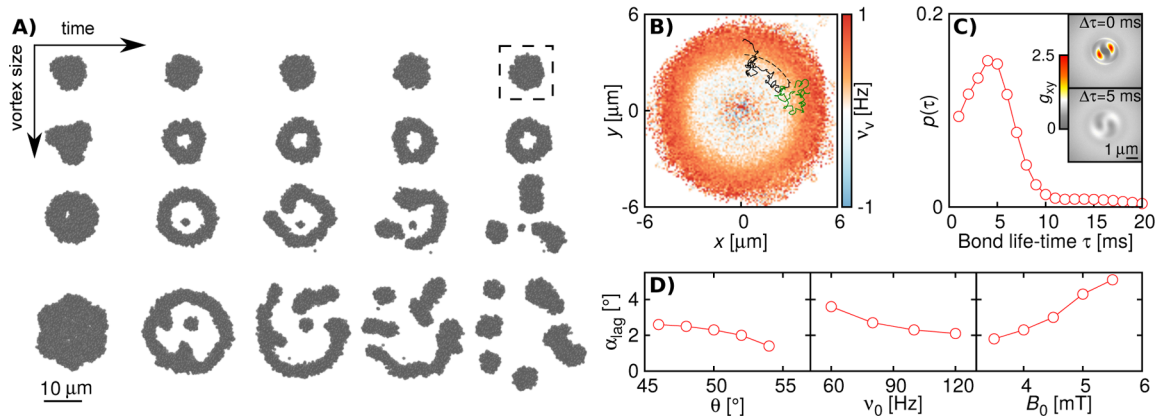
Figure 5. Fluidic steady-state vortices. (A) Simulated time evolution of vortices of various sizes at $\theta = 50°$ and $\nu_0 = 100$ Hz. The smallest vortex remains stable, whereas the larger ones either transform into a hollow cylinder shape or disintegrate into smaller vortices. (B) The 2D velocity profile for the steady-state vortex. The radial velocity profile is clearly inhomogeneous. The short-time trajectories of two particles initially very close together are displayed with solid green and black lines. The black dashed line illustrates the "average" trajectory corresponding to the rotation (for the same duration) of the entire vortex. (C) The steady-state distribution of the bond lifetime τ in the rotating vortex. Two particles are defined as bonded if their interparticle distance is less than 1.2σ. Inset: Spatiotemporal pair correlation function $g_{xy}(\Delta\tau)$ evaluated in the rotating frame of the external field (with field direction parallel to the y axis and rotation anticlockwise). The correlations are shown for time delays of $\Delta\tau = 0$ (top) and 5 ms (bottom). The two correlation plots span an area of 6 μm × 6 μm, and the radial position of the peaks corresponds to two particles in close contact. (D) Lag angle α_{lag} between the external field and the total magnetization of the vortex as a function of field properties θ, ν_0, and B_0. The results in B–D refer to the steady-state vortex marked by a dashed square in plot A.

in time, reminiscent of the sensitivity to the initial conditions in chaotic systems (Figure 5B). The same figure also illustrates the velocity profile in a steady-state vortex, which is proportional to the force density and is clearly inhomogeneous. The simulations show that the internal magnetic interactions lead to a structure in which adjacent particles have a higher probability of being aligned in the direction correlated with the direction of the magnetic field. This is demonstrated by the spatiotemporal correlation function $g_{xy}(\Delta\tau)$ (Figure 5C, inset). The pair correlation in the xy plane is evaluated in the rotating frame of the external field. At $\Delta\tau = 0$, there is a clear peak at the close-contact distance and in the direction lagging behind the external field by about 50°. This correlation decays with time, and it is much less pronounced at $\Delta\tau = 5$ ms. This confirms that inside the vortex, short-lived pairs or chains of particles form and break all the time (Figure S5 and video S6 in the SI). The distribution $p(\tau)$ of the bond lifetime τ is plotted in Figure 5C. There is a pronounced peak at $\tau \approx 5$ ms, about half the period of the external field. The short-lived bonds induce dynamic correlations that result in an effective magnetic anisotropy of the vortex. As a consequence, the direction of the total magnetization of the vortex, $\mathbf{m}_v(t) = \sum_i \mathbf{m}_i(t)$, lags behind the external field $\mathbf{B}_0(t)$. The simulations show that this lag angle is $\alpha_{lag} \approx 2°$ over a broad parameter range (Figure 5D). Finally, the magnetic torque acting on the vortex is $\mathbf{T}_v = \mathbf{m}_v \times \mathbf{B}_0$.

CONTINUUM MODEL OF A VORTEX

To further understand what determines the shape and velocity profile of a vortex, we will now use the driving force obtained from the simulations as an input parameter for a continuum model. We describe the vortex as a ferrofluid with an effective susceptibility $\hat{\chi} = \phi\chi$, where $\phi \approx 0.6$ is the volume fraction of particles in its interior and χ the magnetic susceptibility of a particle. We assume a homogeneous magnetic field inside a cluster. (We neglect local variations of the demagnetizing field.)

To leading order, the effect of the magnetic field on the surface of the cluster can be described with a pressure term

$p_m = \frac{1}{2}\mu_0(\mathbf{M}\cdot\mathbf{n})^2 + \text{const.}$[41] Assuming that the magnetization instantly follows the precessing field (deviations are important for calculating the torque but not the shape), the temporal average of this pressure is

$$\bar{p}_m = \frac{1}{2}\mu_0\hat{\chi}^2 H^2 n_z^2 \left(\frac{3}{2}\cos^2(\theta) - \frac{1}{2}\right) + \text{const} \tag{1}$$

where H denotes the magnetic field strength inside the vortex and n_z is the vertical component of the surface normal. The contributions that are independent of n_z are omitted. Together with the hydrostatic pressure, $p_h = -\phi(\rho-\rho_{H_2O})gz$, the total pressure has to be constant along the surface, which leads to the equation $Cn_z^2 = z + \text{const}$, where

$$C = \frac{\mu_0\hat{\chi}^2 H^2}{2\phi(\rho - \rho_{H_2O})g}\left(\frac{3}{2}\cos^2\theta - \frac{1}{2}\right) \tag{2}$$

We estimate the constant C using the values $\chi = 1.38$,[42] $\rho = 1700$ kg/m^3, $\phi = 0.6$, $\theta = 50°$, and $H = B_0/(\mu_0(1 + \hat{\chi}/3))$ (demagnetizing factor of a sphere). For $B_0 = 3$ mT, we obtain $C = 43$ μm. The solution is stable when $n_z = 0$ close to the bottom of the vortex. If we parametrize the shape as $r(z)$, we obtain the equation

$$\frac{Cr'^2}{1 + r'^2} = z \tag{3}$$

with the solution

$$r(z) = \sqrt{Cz - z^2} + \frac{\pi}{4}C + \frac{C}{2}\arctan\frac{C/2 - z}{\sqrt{Cz - z^2}} - d \tag{4}$$

d denotes a constant that depends on the volume of the cluster. We see that the maximum possible height of a vortex is C and the maximum radius at its base is $\pi C/2$. The maximum volume is $(3\pi^3/16 - \pi/3)C^3$. With a value of $d > 0$, the cluster can be smaller with a pointed tip. Figure 6A,B shows how the clusters
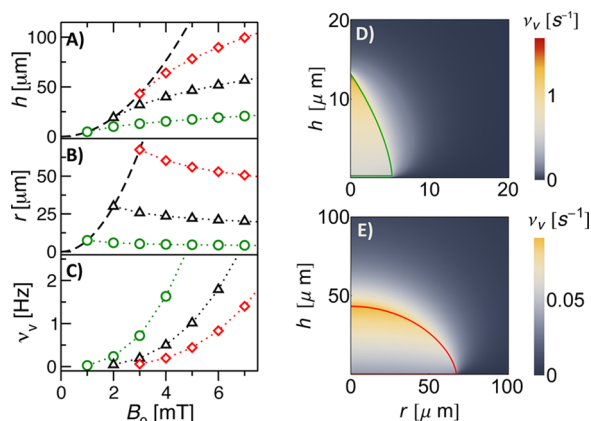
Figure 6. Ferrofluid droplet model of a vortex. (A) Height, (B) basal radius, and (C) average rotational frequency of vortices with different volumes (green circles, 520 μm^3; black triangles, 33 000 μm^3; red diamonds, 380 000 μm^3) as a function of the magnetic field magnitude. Angular velocity profiles inside and outside the cluster at $B_0 = 3$ mT: clusters with a volume of (D) 520 μm^3 and (E) 380 000 μm^3.

with different volumes change their height and basal radius with the magnetic field. The vortices in the experiment were ∼30 μm tall, and the observed basal radii were 4 ± 1 μm (from Figure 4, their cross section is ∼50 μm^2), thus closest to the green symbols in Figure 6. Their nearly constant shape within the observed B_0 range therefore agrees well with the predictions of the ferrofluid droplet model.

The effective driving force obtained from the simulation can be described to a good approximation with a homogeneous torque density $\mathcal{T} = \mu_0 \hat{\chi} H_r^2 \sin \alpha_{lag} \hat{e}_z$. Because of the finite relaxation time of the magnetization, the rotating magnetic field causes an additional torque with a density of

$$\mathcal{T} = \mu_0 \phi \chi''(\omega) H_r^2 \hat{e}_z \qquad (5)$$

where H_r is the rotating component of the magnetic field and $\chi''(\omega)$ is the imaginary part of the susceptibility. In the relevant regime around 100 Hz, χ'' is nearly independent of frequency and has a value of ∼0.035,[35] which corresponds to a lag angle of 1.4°. Interestingly, both contributions to the lag angle are of a similar order of magnitude. We therefore use an effective lag angle of $\alpha_{lag} = 3°$ in the calculation. The torque can be replaced with a force density

$$\mathbf{f} = \frac{1}{2} \nabla \times \mathcal{T} \qquad (6)$$

that results in a tangential force density on the surface of the vortex. We assume that the effective viscosity inside the cluster is 100η (roughly the value for a hard sphere suspension with $\phi = 0.6$[43]) and that there is an additional gap of 0.25 μm between the vortex and the underlying surface. We solve the resulting Stokes equation with an axisymmetric boundary element method. Two examples of velocity profiles are shown in Figure 6D,E. The angular velocity is largely constant radially but grows from the bottom upward. The largest part (55% in Figure 6D, 92% in Figure 6E) of the angular friction on the vortex originates from the gap underneath the vortex. Therefore, the angular velocity of the bottom layer scales approximately with $VH_r^2/r^4 \approx H_r^2 h/r^2$, where h is the height of the vortex and r is its basal radius.

The average rotational frequency of a vortex is shown in Figure 6C. Smaller vortices rotate faster than larger vortices,

and the rotational frequency increases more than quadratically with the magnetic field. Comparing to the experimental results in Figure 4, the frequencies predicted by the ferrofluidic model are larger. It should be noted, however, that the theoretical values are a volumetric average, whereas in the experiment we determined the rotational frequency at the bottom of the vortex where a sharp image could be obtained. Moreover, the model assumptions such as the gap between the vortex and the microscope slide and the value of the magnetization lag angle could not be directly determined in the experiment.

■ DISCUSSION AND CONCLUSIONS

We have presented experiments, theory, and simulations of the emergent dynamic assembly of magnetic colloids in precessing external fields. In a range of parameters, we observe an array of rotating colloidal vortices and explain their stability, which is due to the interplay of several physical mechanisms such as short-lived particle chain formation, many-body-induced interactions, and intraparticle magnetic relaxation. This phase is a dramatic manifestation of dynamic assembly, as the corresponding system with oppressed colloidal dynamics has been shown to assemble into static colloidal membranes.[17] We show that the contributions of magnetic relaxation and structure deformation to the rotation of the vortices are comparable, adding to the complexity of the system. Therefore, we can explain the vortex stability and rotation with two very different approaches. In the simulations, the particles are modeled as magnetically isotropic spheres responding instantly to the external field and hydrodynamic interactions are not fully considered (only as Stokes friction). The main mechanism governing the vortex dynamics is then structural rearrangement, i.e., short-lived chain formation. In the phenomenological ferrofluidic theory, on the other hand, the many-body demagnetization effects are omitted and an effective lag angle of magnetization is used instead.

In our system, the experiments have clearly demonstrated that hydrodynamic effects are negligible on the scale of vortex–vortex interactions. However, more detailed work is in progress in order to fully understand the role of hydrodynamics in dynamic coupling within a single vortex, especially its effect on the transient correlations (short-lived chains) underlying the generation of the torque on the clusters. To compare theory and experiments even more quantitatively, we should note that the phase diagram depends on the particle density, which could not be precisely controlled in the current experiment. Moreover, as pointed out in ref 44, the structures are likely to be sensitive to the details of the short-range repulsive part of the colloidal interactions.

A related emergent behavior has recently been observed in two other systems of a very different nature. In a coarse-grained model of self-propelled particles with memory,[45] a rich variety of collective phases including vortex lattices were observed as a result of the presence of memory in the form of underdamped angular dynamics. In an experimental study of the collective motility of swimming bacteria,[46] a two-dimensional hexagonal lattice of rotating cells was reported and explained with a combination of strong hydrodynamic currents produced by the rotating flagella and steric effects. Although of a different microscopic nature, in those two systems and in the one presented here, angular coupling emerges, which stabilizes an ordered array of rotating structures.

Rotating ribbons or vortices presented in our work could be utilized as a versatile tool for creating vorticity currents in

microfluidic applications. Under the right condition (a very high density of particles) and proper manipulation of the magnetic field, partially disintegrated vortices form arrested structures,[47] which are not accessible through equilibrium assembly routes and can serve as scaffolds for cell growth mimicking the complexity of interactions reminiscent of the organization of life.[48] Moreover, we performed additional experiments where we coated a large spherical bead with micrometer-sized magnetic particles by creating a rotating hollow vortex that sucked in the bead and (upon suppressing the rotation) wrapped it in a one-particle-thick membrane (details in the SI and movie S7). This demonstrates the potential of the observed dynamic phases in particle coating and manipulation applications.

■ MATERIALS AND METHODS

Experiment. An approximately 150-μm-high chamber was filled with an aqueous suspension containing superparamagnetic spheres (diameter 1 μm, Dynal Biotech[42]). The microparticles were coated with BSA (bovine serum albumin, 10 mg/mL) for 4 h in an ultrasonic bath to prevent flocculation. The magnetic field amplitude, direction, and rate of change were controlled by three pairs of semi-Helmholtz coils creating a constant magnetic field component in the z direction and a rotating component in the xy plane. The resulting external magnetic field was precessing on a cone with an opening angle of θ. The magnitude B_0 of the magnetic field was between 2.5 and 6.25 mT, and the precession frequency ν_0 was between 50 and 200 Hz. The particles were initially allowed to sediment at the bottom of the chamber. (The quasi-2D density of the layer formed was between 0.1 and 1 particles per μm^2.) When the magnetic field was turned on, the system assembled into a steady state. All of the results represent a 5.5 s average of a 0.5 mm^2 field of view after the system was left to equilibrate for several minutes. ImageJ[49] was used to analyze the images. The cross-sectional area A_v of the clusters was measured as the number of dark pixels above a threshold gray value. For the vortex rotational frequency, several vortices with a slightly asymmetric shape or a distinctive feature on the outer edge were chosen. The number of frames needed for one rotation was counted and averaged over several rotations. The nonmagnetic pillars (radius 10 μm, height 10 μm) were made from a negative photoresist (SU-8 2025, Microchem, adhesion promoter TI Prime, Microchemicals GmbH) that was structured by direct UV laser illumination (Omikron Laserage GmbH, blue photon LDM375.20.CWA.L, 375 nm, Zeiss LD Plan-neofluar 20 × 0.4 Korr objective) steered by acousto-optic deflectors (A. A. Optoelectronic, DTSXY-400-405) and a beam steering controller (Aresis, BSC-160).

Simulation. We perform Langevin dynamics simulations[50,51] of superparamagnetic colloids in a precessing external magnetic field $\mathbf{B}_{ext}(t) = B_0(\sin\theta\cos 2\pi\nu_0 t, \sin\theta\sin 2\pi\nu_0 t, \cos\theta)$ with magnitude B_0, frequency ν_0, and opening angle θ. Colloids are modeled as hard spheres (repulsive Weeks−Chandler−Andersen potential[52]) of diameter σ with an induced pointlike magnetic moment in the center. The magnetic dipole

$$\mathbf{m}_i = \frac{4\pi\sigma^3\chi}{24\mu_0}\mathbf{B}_{loc}(\mathbf{r}_i)$$

of the ith particle is proportional to the local magnetic field, i.e., the external field plus depolarization contributions of other dipoles

$$\mathbf{B}_{loc}(\mathbf{r}_i) = \mathbf{B}_{ext} + \frac{\mu_0}{4\pi}\sum_j\frac{3(\mathbf{m}_j(t)\cdot\hat{r}_{ij})\hat{r}_{ij} - \mathbf{m}_j(t)}{r_{ij}^3}$$

Here, μ_0 is the vacuum permeability and χ is the magnetic susceptibility of the colloidal particles. The colloidal particles are assumed to be magnetically isotropic and to have an instantaneous response to the external field. A self-consistent procedure was adopted to solve the above equations and compute the magnetic moments $\mathbf{m}_i(t)$ for every configuration. The total force on a particle is composed

of the interparticle term $\mathbf{F}_{int} = \mathbf{F}_{dipole} + \mathbf{F}_{WCA}$, the hydrodynamic drag $\mathbf{F}_{hydro} = -\gamma\mathbf{v} = -6\pi\eta\frac{\sigma}{2}\mathbf{v}$ with η being the fluid viscosity and $\mathbf{v}$ being the particle velocity, and a random contribution to account for thermal fluctuations $\mathbf{F}_{fluc}$ satisfying (i) $\langle\mathbf{F}_{fluc}\rangle = 0$ and (ii) $\langle\mathbf{F}_{fluc}(t)\,\mathbf{F}_{fluc}(t')\rangle = 6k_BT\gamma\delta(t-t')$, where γ is a Gaussian distributed function with a zero average and a variance of 1. We have used the following parameters corresponding to the experimental system: $\chi = 1.3$, $T = 300$ K, $\epsilon_{WCA} = 40\,k_BT$, $\sigma = 1\,\mu$m, mass of the particle 10^{-15} kg, and $\eta = 0.001$ Pa s. Periodic boundary conditions were applied in all three dimensions, and the minimum image convention was used to compute the forces. To account for the long-range effects of magnetic interactions, we adopted the method of Lorentz,[53] which has been used in similar studies in the past.[4−7]

■ ASSOCIATED CONTENT

Ⓢ Supporting Information
The Supporting Information is available free of charge on the ACS Publications website at DOI: 10.1021/acs.langmuir.6b00722.

> Vortex phase, stability of static structures, role of hydrodynamic forces, steady-state dynamics, vortex dynamics at a single-particle level, particle coating experiment, and list of supplemental movies (PDF)
> Movies illustrating membrane disintegration, material exchange, pillar, steady state, vortex dynamics, and particle coating (ZIP)

■ AUTHOR INFORMATION

Corresponding Author
*E-mail: jd489@cam.ac.uk.

Author Contributions
T.M. and G.K. contributed equally.

Notes
The authors declare no competing financial interest.

■ ACKNOWLEDGMENTS

■ REFERENCES

(1) Solis, K. J.; Martin, J. E. Complex magnetic fields breathe life into fluids. *Soft Matter* **2014**, *10*, 9136−9142.

(2) Martin, J. E.; Solis, K. J. Symmetry-breaking magnetic fields create a vortex fluid that exhibits a negative viscosity, active wetting, and strong mixing. *Soft Matter* **2014**, *10*, 3993−4002.

(3) Solis, K. J.; Martin, J. E. Torque density measurements on vortex fluids produced by symmetry-breaking rational magnetic fields. *Soft Matter* **2014**, *10*, 6139−6146.

(4) Martin, J. E.; Anderson, R. A.; Williamson, R. L. Generating strange magnetic and dielectric interactions: Classical molecules and particle foams. *J. Chem. Phys.* **2003**, *118*, 1557−1570.

(5) Martin, J. E.; Venturini, E.; Gulley, G. L.; Williamson, J. Using triaxial magnetic fields to create high susceptibility particle composites. *Phys. Rev. E* **2004**, *69*, 021508.

(6) Martin, J. E.; Venturini, E.; Odinek, J.; Anderson, R. A. Anisotropic magnetism in field-structured composites. *Phys. Rev. E* **2000**, *61*, 2818−2830.

(7) Martin, J. E.; Anderson, R. A.; Tigges, C. P. Simulation of the athermal coarsening of composites structured by a biaxial field. *J. Chem. Phys.* **1998**, *108*, 7887−7900.

(8) Snezhko, A.; Belkin, M.; Aranson, I. S.; Kwok, W.-K. Self-Assembled Magnetic Surface Swimmers. *Phys. Rev. Lett.* **2009**, *102*, 118103.

(9) Belkin, M.; Snezhko, A.; Aranson, I. S.; Kwok, W.-K. Driven Magnetic Particles on a Fluid Surface: Pattern Assisted Surface Flows. *Phys. Rev. Lett.* **2007**, *99*, 158301.

(10) Snezhko, A.; Aranson, I. S.; Kwok, W.-K. Surface Wave Assisted Self-Assembly of Multidomain Magnetic Structures. *Phys. Rev. Lett.* **2006**, *96*, 078701.

(11) Kokot, G.; Piet, D.; Whitesides, G. M.; Aranson, I. S.; Snezhko, A. Emergence of reconfigurable wires and spinners via dynamic self-assembly. *Sci. Rep.* **2015**, *5*, 9528.

(12) Ray, A.; Aliaskarisohi, S.; Fischer, T. M. Dynamics of self-assembly of flower-shaped magnetic colloidal clusters. *Phys. Rev. E* **2010**, *82*, 031406.

(13) Tierno, P.; Muruganathan, R.; Fischer, T. M. Viscoelasticity of Dynamically Self-Assembled Paramagnetic Colloidal Clusters. *Phys. Rev. Lett.* **2007**, *98*, 028301.

(14) Tierno, P.; Johansen, T. H.; Fischer, T. M. Fast and rewritable colloidal assembly via field synchronized particle swapping. *Appl. Phys. Lett.* **2014**, *104*, 174102.

(15) Tierno, P. Recent advances in anisotropic magnetic colloids: realization, assembly and applications. *Phys. Chem. Chem. Phys.* **2014**, *16*, 23515−23528.

(16) Tierno, P. Depinning and Collective Dynamics of Magnetically Driven Colloidal Monolayers. *Phys. Rev. Lett.* **2012**, *109*, 198304.

(17) Osterman, N.; Poberaj, I.; Dobnikar, J.; Frenkel, D.; Ziherl, P.; Babić, D. Field-Induced Self-Assembly of Suspended Colloidal Membranes. *Phys. Rev. Lett.* **2009**, *103*, 228301.

(18) Vilfan, M.; Potočnik, A.; Kavčič, B.; Osterman, N.; Poberaj, I.; Vilfan, A.; Babić, D. Self-assembled artificial cilia. *Proc. Natl. Acad. Sci. U. S. A.* **2010**, *107*, 1844−1847.

(19) Albrecht, M.; Maier, A.; Treubel, F.; Maret, M.; Poinsot, R.; Schatz, G. Self-assembled magnetic nanostructures of $CoPt_3$ with favoured chemical ordering. *EPL* **2001**, *56*, 884.

(20) Martin, J. E.; Snezhko, A. Driving self-assembly and emergent dynamics in colloidal suspensions by time-dependent magnetic fields. *Rep. Prog. Phys.* **2013**, *76*, 126601.

(21) Kulić, I. M.; Kulić, M. L. Self-Assembly of Colloidal Superstructures in Coherently Fluctuating Fields. *Phys. Rev. Lett.* **2013**, *111*, 198301.

(22) Kulić, I. M.; Kulić, M. L. Theory of coherent van der Waals matter. *Phys. Rev. E* **2014**, *90*, 062313.

(23) Müller, K.; Osterman, N.; Babić, D.; Likos, C. N.; Dobnikar, J.; Nikoubashman, A. Pattern Formation and Coarse-Graining in Two-Dimensional Colloids Driven by Multiaxial Magnetic Fields. *Langmuir* **2014**, *30*, 5088−5096.

(24) Angioletti-Uberti, S.; Mognetti, B. M.; Frenkel, D. Re-entrant melting as a design principle for DNA-coated colloids. *Nat. Mater.* **2012**, *11*, 518−522.

(25) Yan, J.; Bae, S. C.; Granick, S. Rotating crystals of magnetic Janus colloids. *Soft Matter* **2015**, *11*, 147−153.

(26) Chaudhary, K.; Juarez, J. J.; Chen, Q.; Granick, S.; Lewis, J. A. Reconfigurable assemblies of Janus rods in AC electric fields. *Soft Matter* **2014**, *10*, 1320−1324.

(27) Yan, J.; Bloom, M.; Bae, S. C.; Luijten, E.; Granick, S. Linking synchronization to self-assembly using magnetic Janus colloids. *Nature* **2012**, *491*, 578−581.

(28) Solis, K. J.; Martin, J. E. Isothermal Magnetic Advection: Creating functional fluid flows for heat and mass transfer. *Appl. Phys. Lett.* **2010**, *97*, 034101.

(29) Snezhko, A. Non-equilibrium magnetic colloidal dispersions at liquid-air interfaces: dynamic patterns, magnetic order and self-assembled swimmers. *J. Phys.: Condens. Matter* **2011**, *23*, 153101.

(30) Snezhko, A.; Aranson, I. S. Magnetic manipulation of self-assembled colloidal asters. *Nat. Mater.* **2011**, *10*, 698−703.

(31) Dobnikar, J.; Snezhko, A.; Yethiraj, A. Emergent colloidal dynamics in electromagnetic fields. *Soft Matter* **2013**, *9*, 3693−3704.

(32) Timonen, J. V. I.; Latikka, M.; Leibler, L.; Ras, R. H. A.; Ikkala, O. Switchable Static and Dynamic Self-Assembly of Magnetic Droplets on Superhydrophobic Surfaces. *Science* **2013**, *341*, 253−257.

(33) Hermans, T. M.; Frauenrath, H.; Stellacci, F. Droplets Out of Equilibrium. *Science* **2013**, *341*, 243−244.

(34) Bai, H.; Chen, Y.; Delattre, B.; Tomsia, A. P.; Ritchie, R. O. Bioinspired large-scale aligned porous materials assembled with dual temperature gradients. *Science Advances* **2015**, *1*, e1500849.

(35) Janssen, X.; Schellekens, A.; van Ommering, K.; van IJzendoorn, L.; Prins, M. W. J. Controlled torque on superparamagnetic beads for functional biosensors. *Biosens. Bioelectron.* **2009**, *24*, 1937.

(36) Tierno, P.; Claret, J.; Sagués, F.; Cēbers, A. Overdamped dynamics of paramagnetic ellipsoids in a precessing magnetic field. *Phys. Rev. E* **2009**, *79*, 021501.

(37) Lenz, P.; Joanny, J.-F.; Jülicher, F.; Prost, J. Membranes with Rotating Motors. *Phys. Rev. Lett.* **2003**, *91*, 108104.

(38) Skotheim, J. M.; Mahadevan, L. Soft Lubrication. *Phys. Rev. Lett.* **2004**, *92*, 245509.

(39) Grzybowski, B. A.; Stone, H. A.; Whitesides, G. M. Dynamic self-assembly of magnetized, millimetre-sized objects rotating at a liquid−air interface. *Nature* **2000**, *405*, 1033−1036.

(40) Llopis, I.; Pagonabarraga, I. Hydrodynamic regimes of active rotators at fluid interfaces. *Eur. Phys. J. E: Soft Matter Biol. Phys.* **2008**, *26*, 103−113.

(41) Rosensweig, R. *Ferrohydrodynamics*; Dover Publications: Mineola, NY, 1997.

(42) Fonnum, G.; Johansson, C.; Molteberg, A.; Mørup, S.; Aksnes, E. *J. Magn. Magn. Mater.* **2005**, *293*, 41−47.

(43) van der Werff, J. C.; de Kruif, C. G. Hard-sphere Colloidal Dispersions: The Scaling of Rheological Properties with Particle Size, Volume Fraction, and Shear Rate. *J. Rheol.* **1999**, *33*, 421.

(44) Richardi, J.; Weis, J.-J. Low density mesostructures of confined dipolar particles in an external field. *J. Chem. Phys.* **2011**, *135*, 124502.

(45) Nagai, K. H.; Sumino, Y.; Montagne, R.; Aranson, I. S.; Chaté, H. Collective Motion of Self-Propelled Particles with Memory. *Phys. Rev. Lett.* **2015**, *114*, 168001.

(46) Petroff, A. P.; Wu, X.-L.; Libchaber, A. Fast-Moving Bacteria Self-Organize into Active Two-Dimensional Crystals of Rotating Cells. *Phys. Rev. Lett.* **2015**, *114*, 158102.

(47) Kokot, G.; Zemljič Jokhadar, Š.; Batista, U.; Babić, D. Magnetically Self-Assembled Colloidal Three-Dimensional Structures as Cell Growth Scaffold. *Langmuir* **2015**, *31*, 9576−9581.

(48) Alon, U. *An Introduction to Systems Biology: Design Principles of Biological Circuits*; Chapman & Hall/CRC Mathematical and Computational Biology Series; Chapman & Hall/CRC, 2007.

(49) Schneider, C. A.; Rasband, W. S.; Eliceiri, K. W. NIH Image to ImageJ: 25 years of image analysis. *Nat. Methods* **2012**, *9*, 671−675.

(50) Sivak, D. A.; Chodera, J. D.; Crooks, G. E. Using Non-equilibrium Fluctuation Theorems to Understand and Correct Errors in Equilibrium and Nonequilibrium Simulations of Discrete Langevin Dynamics. *Phys. Rev. X* **2013**, *3*, 011007.

(51) Sivak, D. A.; Chodera, J. D.; Crooks, G. E. Time Step Rescaling Recovers Continuous-Time Dynamical Properties for Discrete-Time Langevin Integration of Nonequilibrium Systems. *J. Phys. Chem. B* **2014**, *118*, 6466−6474.

(52) Weeks, J. D.; Chandler, D.; Andersen, H. C. Role of Repulsive Forces in Determining the Equilibrium Structure of Simple Liquids. *J. Chem. Phys.* **1971**, *54*, 5237−5247.

(53) Tao, R.; Sun, J. M. Three-dimensional structure of induced electrorheological solid. *Phys. Rev. Lett.* **1991**, *67*, 398−401.